ETH

Eidgenössische Technische Hochschule Zürich
Swiss Federal Institute of Technology Zurich

Pseudo-3D Ground Penetrating Radar imaging of past and present landslides in the Urserental

Bachelor Thesis

Ria Fischer

Supervisors:

Dr. Stefan Carpentier

Dipl.-Geophys. Heinrich Horstmeyer

Department of Earth Sciences, Institute of Geophysics

Zurich, July 2010

I. Abstract

If one goes up to the Urserental which lays in the heart of the Swiss Central Alps, the northern slope will catch a watchful observer's eye instantly. The whole slope is covered in landslides of different stages. In the study area alone, which lies in the northern slope half a kilometre above Hospental near Andermatt, there can be found three different stages of landslides.

With the help of narrowly spaced 100MHz and 250MHz Ground Penetrating Radar (GPR) lines, soil profiles and a topography analysis a highly complex landslide system could be detected. In the steeper part soil is slowly built up and the calcareous bedrock and wet climate encourage the building of a clay layer which acts as a gliding plane for landslides. The landslides creep downhill in a slow part by part movement until certain conditions are met and failure occurs. They are then deposited in the flatter part where multiple landslides are stacked indicated by the finding of multiple clay layers. Finally this system seems to propagate westwards along the slope.

A detailed understanding of the sliding mechanism is the first important step in a successful mitigation of landslide risk [*Lacasse and Nadim*, 2009]. Therefore this thesis might also provide its small part in making the Urserental more habitable and cultivatable.

II.   Contents

III.   Acknowledgment

1   Introduction

1.1   Motivation

If one goes up to the Urserental, which lays in the heart of the Swiss Central Alps, the northern slope will catch a watchful observer's eye instantly: A huge part of it is covered in landslides. The study area covered by this thesis is a roughly 160m x 160m wide part of the northern slope and about 500m away from Hospental containing different stages of landslides. Actively creeping areas are recognised by cracks in the ground and folding of the top soil (see figure 1.1 the black arrows). Most noticeable are also the past landslide areas where most of the top soil and vegetation is missing and is growing back only slowly.

Landslides in general can pose a threat to human life and damage property, infrastructure or agricultural land. There has also to be taken into account the soil loss resulting from landslides [*K. Meusburger and Alewell*, 2008].

In the specific case of the Urserental most villages, like Hospental at the investigation site, are built on the opposite side of the valley at the foot of the southern slope. This reduces the risk of damage to people. Nevertheless, there are a couple of farm houses as well as infrastructure like roads or water and power supply which are threatened by landslide activity, and the surrounding farm land which suffers from the afore-mentioned soil loss. Due to a landslide most of the top soil and vegetation is removed, which leads to the land being waste for pasturing or haying.

1.2   Main goals

Due to Lacasse and Nadim [2009] the first step for a successful mitigation of landslide risk is the precise description of the landslide build-up and the surrounding area as well as the sliding mechanism and possible triggers. Thus the main goals of this study are as follow.

In a first part of this thesis the build-up of 'pre-landslides' are described, as well as their settling into the surrounding landscape. The term 'pre-landslide' here signifies an already unstable part of soil or underground which has not yet shown clear failure.

In the second part a possible sliding mechanism is deduced from the observed build-up. Two fundamentally different mechanisms are discussed at this stage, one extreme being a steady and slow creeping motion, the other one being a part by part motion with cracks opening and closing in the process. It is assumed that a clay or loam layer acts as a gliding plane as this is usually the case with landslides.

In a later study a water-flow and –storage model will be proposed for the observed clay layer. This model should be able to predict the time of failure in relation to the precipitation. It is assumed from earlier measurements that there are steps or pockets in the topography of the clay layer which can store precipitation up to a critical amount and when a certain limit is reached failure occurs.
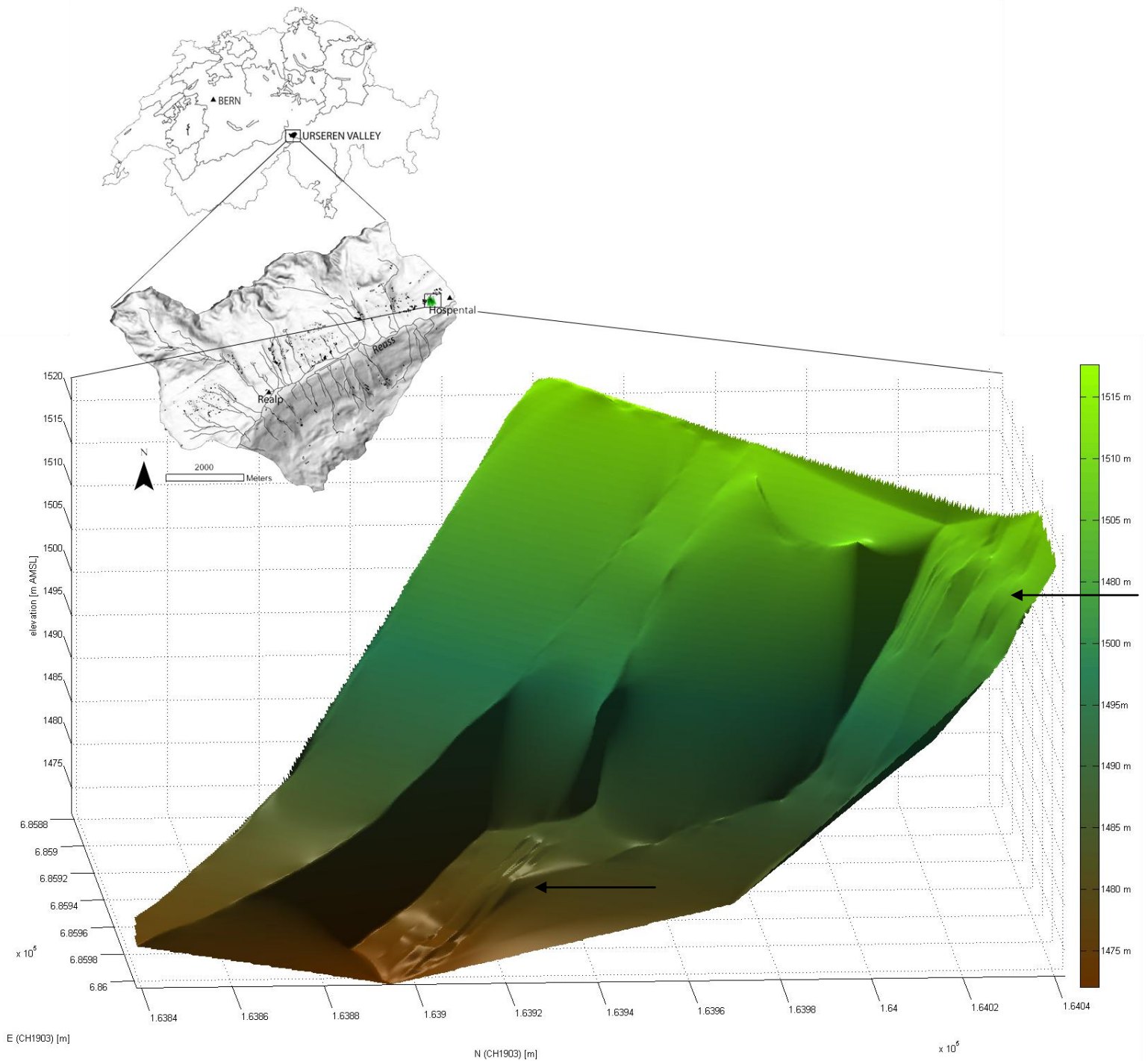
Figure 1.1: Urserental, elevation model of the study area. Note the fairly large variation in slope and the subtle small bumps marked with black arrows. Both topographic features are connected with landslide activity.
(Map Switzerland and Urserental modified from Meusburger and Alewell [2009])

2 Geologic Setting

2.1 General situation

The subsequent section follows Pfiffner [2009]. The geology of the northern central Alps is mostly dominated by two big massifs: The Aare massif and the Gotthard massif. These two massifs are part of the parautochthonous crystalline basement of the Helvetic zone and partially overthrusted for a few kilometres. The bodies of both massifs are composed of old Variscian high metamorphic rocks and granitic intrusions of Palaeozoic age (Tödi Granite for the Gotthard massif, Central Aare Granite for the Aare massif). The cover of Permian and Triassic sediments was sheared off during Alpine orogeny along the Axen fault among others. It is unclear where the sediments have been transported to, but they now build part of the Helvetic nappes in the Central Alps (Axen-, Diablerets-, Gellihorn nappe). The Aare massif is thrusted over the autochthonous crystalline foreland and the Gotthard massif is thrusted over the Aare massif along the Axen fault. The massifs are separated by a Permian and Triassic sediment streak. This sediment zone is called the Urseren Zone.

2.2 Urseren Zone and Urserental

The Urseren Zone is a sediment wedge which streaks more or less NNE – SSW and dips 60°-90° to the north. It is built up from rocks like marble, calcareous schist, phyllitic shale and dolomite [*Fehr*, 1926].

The Urserental follows almost perfectly the Urseren Zone. The southern slope of the valley is built up by the Gotthard massif, the northern slope is built up by the Aare massif and the valley bottom and the lower part of the northern slope are built up from rocks of the Urseren Zone. From South to North younger rocks are exposed (see figure 2.2). After Fehr [1926] the study area lays in Permian Verrucano, built from rhyolite and chlorite schist, sericite schist, conglomerate gneiss. This is affirmed by the rocks found at the study area: most likely calcareous shale and conglomerate gneiss. In the past landslide mass mostly sericite or chlorite schist was found.
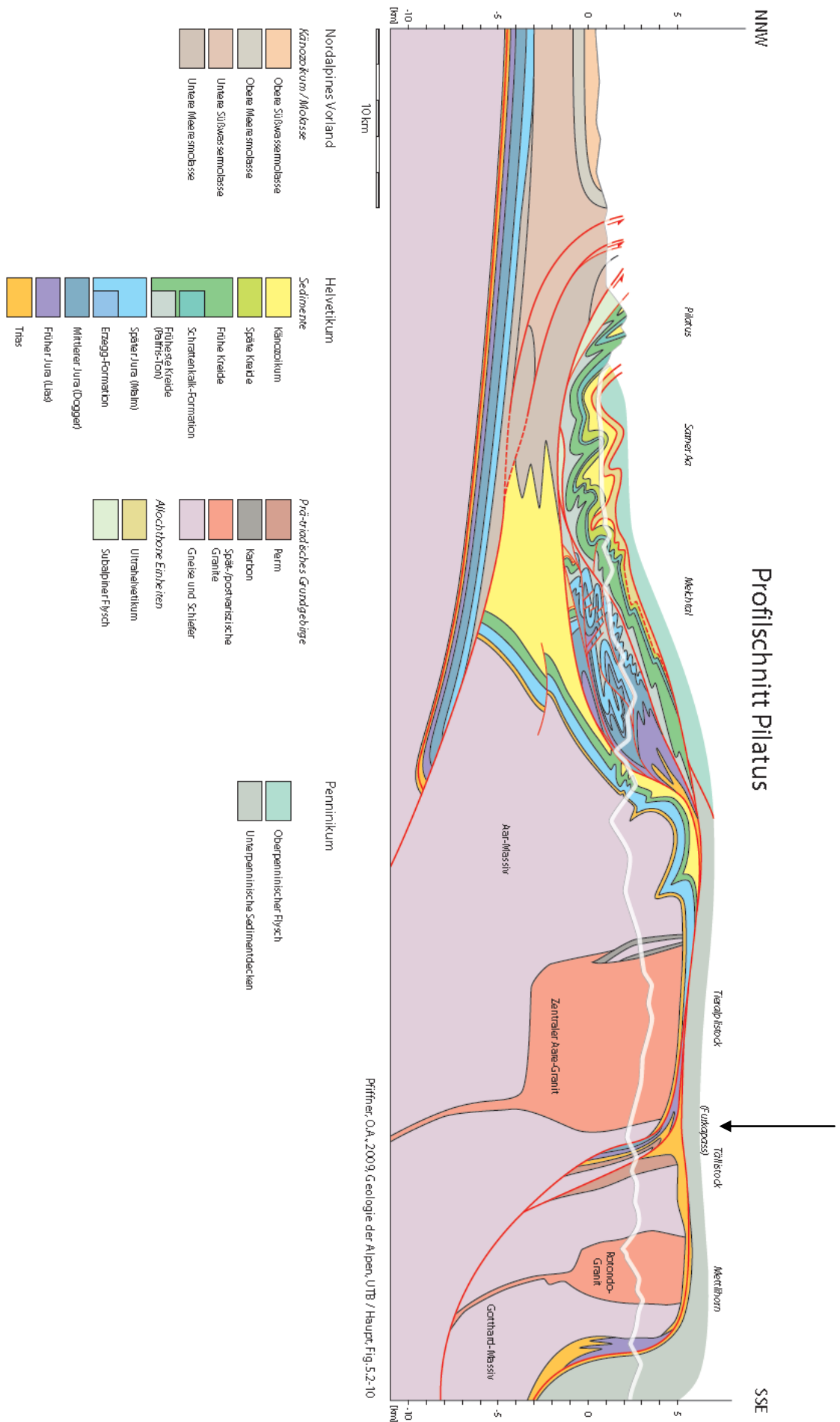
Figure 2.1: Profile through the Helvetic zone (northern Alps): Mount Pilatus-Furkapass. The black arrow marks the location of the Urserental.
[*Pfiffner*, 2009]
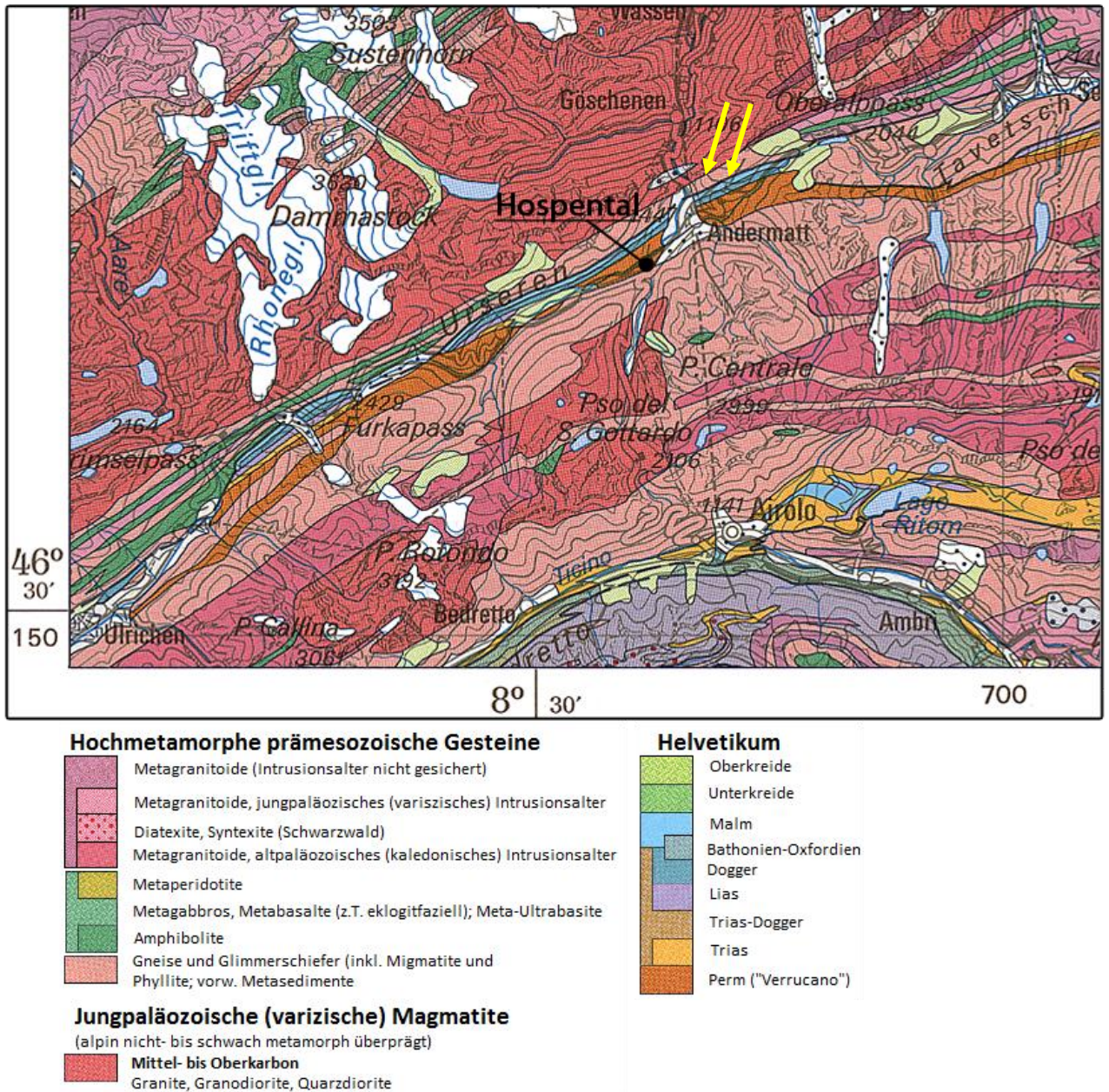
Figure 2.2: Geological map of the Urserental. The two faults near Hospental are marked with yellow arrows.
[Institut für Geologie der Universität Bern, 2005]

2.3 Quaternary

As already mentioned above, the Urseren Zone forms a wedge of softer sediments between the more compatible crystalline rocks of the Aare and the Gotthard massif. This zone of soft sediments was eroded by the Reuss glacier during the Riss and mostly the Würm glaciations, carving out the Urseren valley [*Cadisch et al.*, 1948]. Remnants of these glaciations can be found all over the valley in form of moraines and roches moutonnées.

The present face of the valley though was completed by the river Reuss digging its path deep into the valley bottom and by rock falls and landslides eroding the steep slopes and these processes are still going on.

In the majority of cases a clay layer acts as a gliding plain for landslides, which could also very well be the case in the Urserental. The mica, shale and marble of the Urseren Zone tend to weather to clay under the influence of water. This could be a reason why the dominant soil types in the valley are Podsols and Cambisols [*Katrin Meusburger*, 2009]. These soil types can be recognised by the eluviation of clay and iron in the highly acidic environment and the subsequent building of a clay layer and rust spots [*Blume et al.*, 2002].

3 Materials and methods

3.1 Ground Penetrating Radar (GPR)

In this study the GPR method was favoured for its high resolution and still acceptably fast acquisition speed. Other possible methods would have been high-resolution seismics with the disadvantage of being quite time-consuming or geoelectrics with higher acquisition speed but data in only low-resolution.

3.1.1 Basic principles

This next section is motivated by Annan [2009]. GPR is a non-destructive and nowadays widely used geophysical method. Electromagnetic waves in a spectrum between 10 to 1000 MHz are used to examine the shallow subsurface. GPR is based on the electromagnetic (EM) theory. Electromagnetic phenomena can be explained by the Maxwell's equations:

$$\overline{\nabla} \times \overline{E} = -\frac{\partial \overline{B}}{\partial t} \tag{3.1}$$

$$\overline{\nabla} \times \overline{H} = \overline{J} + \frac{\partial \overline{D}}{\partial t} \tag{3.2}$$

$$\overline{\nabla} \cdot \overline{D} = q \tag{3.3}$$

$$\overline{\nabla} \cdot \overline{B} = 0 \tag{3.4}$$

where E is the electrical field in (V/m); B is the magnetic induction field in (T or Wb/m^2); t is time in (s); H is the magnetic field strength in (A/m); J is electric current density in (A/m^2); D is the electric displacement field in (C/m^2); q is electric charge density in (C/m^3).

The constitutive equations link together J and E, D and E, and B and H by use of the material properties σ, ε and μ:

$$\overline{J} = \sigma \overline{E} \tag{3.5}$$

$$\overline{D} = \varepsilon \overline{E} \tag{3.6}$$

$$\overline{B} = \mu \overline{H} \tag{3.7}$$

where σ is the electrical conductivity in (S/m); ε is the dielectric permittivity in (F/m); μ is the magnetic permeability in (H/m). The magnetic permeability μ is usually of minor importance. Of greater interest in GPR applications are the variations in σ and $\varepsilon_r = \frac{\varepsilon}{\varepsilon_0}$, where ε_0 is the permittivity of vacuum and ε_r is the relative permittivity. In most GPR issues they are treated as field independent and constant.

Relative permittivity ε_r depends on the water content and reaches a spectrum between 1 for air and 80 for water. Electrical conductivity σ depends on the free charge movement and reaches a spectrum between 0mS/m for air, 0.01mS/m for ice, dry salt and distilled water up to 3000mS/m for sea water.

This enables GPR technique to image special structures like a clay layer for its high rate of free charge movement or also the water table or the bedrock for its strong contrast in water content.

GPR makes use of the wave character of EM fields. By combining Maxwell's and the constitutive equations, a set of two new equations can be obtained for the electric and the magnetic field:

$$\nabla^2 E - \varepsilon\mu\frac{\partial^2 E}{\partial t^2} - \sigma\mu\frac{\partial E}{\partial t} = 0 \qquad (3.8)$$

$$\nabla^2 H - \varepsilon\mu\frac{\partial^2 H}{\partial t^2} - \sigma\mu\frac{\partial H}{\partial t} = 0 \qquad (3.9)$$

The GPR device usually measures the electric (E) field and is most effective in environments with small energy dissipation compared to energy storage.

By solving the differential equations above, three key wave field expressions can be obtained:

$$v = \frac{1}{\sqrt{\varepsilon\cdot\mu}} = \frac{c}{\sqrt{\varepsilon_r}} \qquad (3.10)$$

$$\alpha = \sqrt{\frac{\mu}{\varepsilon}}\cdot\frac{\sigma}{2} = Z_0\cdot\frac{\sigma}{2\cdot\sqrt{\varepsilon_r}} \qquad (3.11)$$

$$Z = \sqrt{\frac{\mu}{\varepsilon}} = \frac{Z_0}{\sqrt{\varepsilon_r}} \qquad (3.12)$$

where v is velocity in (m/s), α is attenuation in (m^{-1}) and Z is impedance in (Ω). At high frequencies, like the ones used in GPR, the common agreement is that these properties are approximately constant within the frequency bandwidth of a GPR pulse.

The following rules apply for frequency:

$$\Delta r = \frac{\lambda}{4} \quad \rightarrow \quad \Delta r \sim \frac{1}{f} \qquad (3.13)$$

$$d \sim \frac{1}{f} \qquad (3.14)$$

where λ is wavelength in (m), f is frequency in (Hz), Δr is range or vertical resolution in (m) and d is depth penetration in (m). Formula (3.13) is known as the Rayleigh criterion. From these two equations can be gathered that there is a trade-off between frequency and resolution and frequency and depth penetration. The higher the frequency is set the higher a possible resolution will be but the lower the depth penetration. This has to be taken into account when the surveying frequency is chosen.

3.1.2 Acquisition setup

The data was acquired with a 250MHz and a 100MHz GPR device. In figure 3.1 data acquisition with a 100MHz GPR is shown. Figure 3.2 shows the measuring situation schematically. A1 marks the measuring GPS antenna, A2 the base station, A3 the second GPS antenna for time coordination and A4 a GPS satellite necessary for the measurements, but the DGPS system will be explained in the next chapter. The data was acquired with the common-offset method. This requires transmitter B1 and receiver B2 to always have the same constant distance (see table 3.1: antenna distance). This transmitter-receiver couple is then moved along a line where either in the case with the 100MHz device as many measurements are taken as possible with the limiting factor being the console or in the case of the 250MHz device a wheel triggers the measurements after a certain distance. The signal goes into the subsurface (C) and is reflected back to the receiver (D) at interfaces with high impedance contrast (formula (3.12)). It is then stored and processed by the console (E).

Figure 3.1: Measuring situation with the 100MHz GPR device.
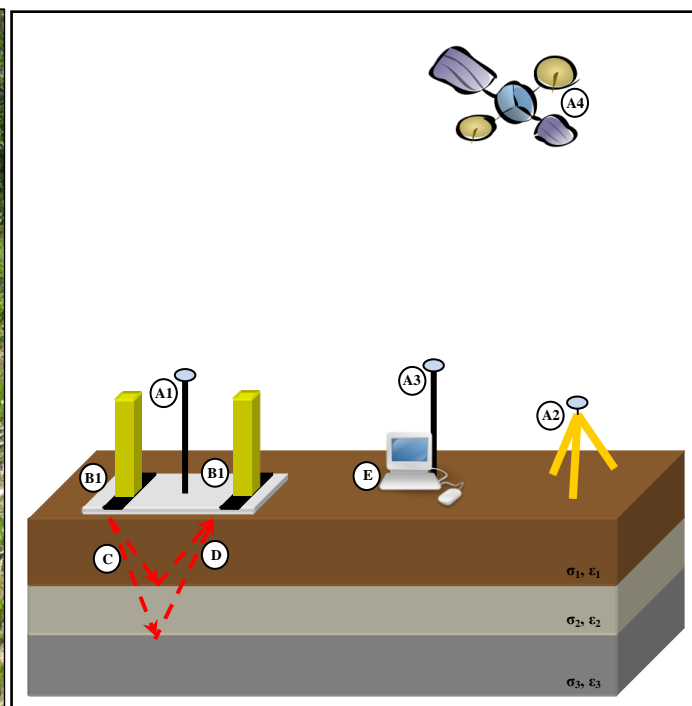
Figure 3.2: Schematic measuring situation for GPR data acquisition.

3.1.3 Data acquisition

The GPR data used in this thesis was collected in summer 2009 with a 100MHz and a 250MHz PulseEKKO GPR device. The study area can be divided into two main parts: A lower flatter part (labelled L in figure 3.3) and an upper steeper part (areas U1-U3). The upper part is split by a past landslide from spring or early summer 2008 dividing it into three separate parts: The part left of the landslide (U1), the part with the past landslide with rather rough terrain (U2) and the part right of the landslide (U3). Three long lines a1 to a3 and one long cross line a4 were collected with the 100MHz device for an overview. Also with the 100MHz device eleven short lines were collected in the steep part. Lines a9 and a13 to a15 were collected in area U1. Line a10 was collected over the past landslide in area U2, which rushed down in spring 2008 and lines a5 to a8 were collected right of the past landslide in area U3. Lines a5 to a7 are discarded for disrupted GPS measurements. Five more short lines, a16 to a20, were collected at the shallower bottom part in area L.

With the 250MHz device seven short lines, b1 to b7, were collected in area U1, one line b11 was collected in area U2 and three lines b8 to b10 were collected right of the past landslide in area U3. At the shallow bottom part in area L five lines b12 to b16 were collected. For an overview see Table 8.1. Also Table 3.1 summarises the essential parameters.

	a1-a20	b1-b16
frequency	100MHz	250MHz
sample rate	0.8ns	0.4ns
samples per trace	500	500
trace spacing	0.2m	0.05m
antenna distance	1.0m	0.40m
measuring scheme	free run	triggered
stacking	32	16
recording length	400ns	200ns

Table 3.1: Essential measuring parameters for the 100MHz and 250MHz datasets

Another measuring campaign on February 6th 2010, with the objective of gathering enough data for full 3D-processing, yielded mostly corrupt results: most of the recorded lines showed massive reverberations. A cause could be either the snow cover or interference between GPS and GPR antenna.
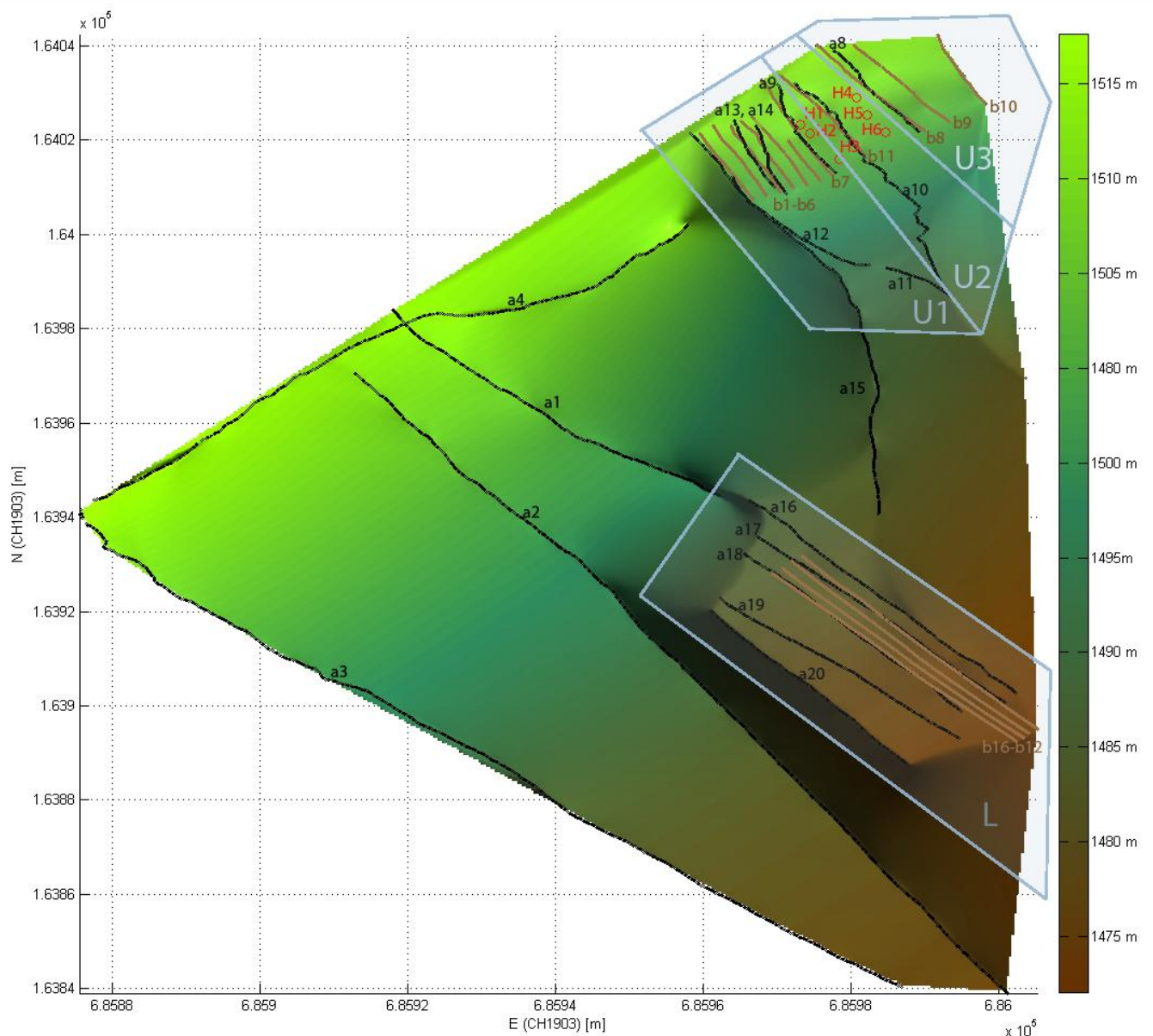
Figure 3.3: Map of the investigation area showing elevation in green and brown colours. The black lines a1-a20 signify measurements with the 100MHz GPR device, lines in brown b1-b16 signify measurements with the 250MHz GPR device. Points H1-H6 mark the spots where the soil profiles where taken. The grey patch L marks the lower part, the upper grey part can be divided into a part U2 with a past landslide which went down spring/summer 2008, a part left of it(U1) which is probably actively creeping and a part right of the past landslide (U3).

3.1.4 Data processing
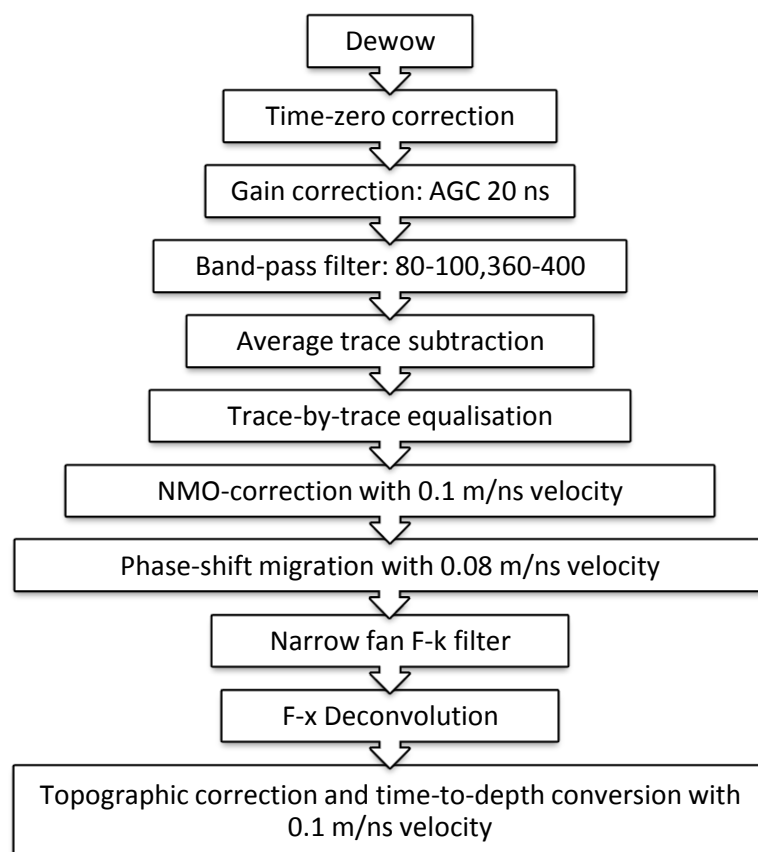
Figure 3.4: Sketch of the processing steps and figures for the 250MHz dataset

3.1.4.1 Dewow

First the raw data is checked for any missing or swapped headers or lines, and if any are found, the corresponding data is mended or blanked if necessary.

Then corrupted or blank traces are removed. Causes can be by external noise, equipment failure or too fast movement of the device [*Cassidy*, 2009].

For the actual dewow processing step the 'wow'-effect, a bias towards low frequencies, is removed. For each trace a constant DC offset is subtracted first. Then the remaining extremely low frequency component is removed again for each trace separately.

3.1.4.2 Time-zero correction

Various causes, like thermal drift or electronic instability [*Cassidy*, 2009], can procure jumps in the first arrival time, which is called the time-zero point. This has to be corrected for by setting a common time-zero position. This also leads to the air wave being cut off.

3.1.4.3 Gain correction

Gain correction works as an amplitude compensation and thus improves the visual form of a GPR profile by enhancing the appearance of later arrivals, which have been diminished by the effects of geometrical spreading or attenuation. There are different types of functions and time windows to choose from but all of them work in the same manner. A time window slides along each trace and at each position the values in the window are multiplied by a certain factor.

Automatic gain control (AGC) with a time window of 20ns was applied. AGC tends to amplify weak deeper events but also noise, therefore has to be applied with care.

3.1.4.4 Band-pass filter

A band-pass filter is a frequency-domain filter, which cuts off low and high frequencies likewise. What remains is a 'band' of the favoured frequencies.

For the 250MHz dataset frequencies 80-100MHz and 360-400MHz were defined as edges of the frequency band function. This leads to frequencies smaller 80MHz and higher 400MHz being removed totally and frequencies in the edge frequency bands being partially removed.

3.1.4.5 Average trace subtraction

To suppress horizontal stripes average trace subtraction was applied. The goal of this method is to reduce high amplitude peaks in single traces. This is done by summing up several adjacent traces and subtracting the mean value from each one.

3.1.4.6 Trace-by-trace equalisation

Trace-by-trace equalisation acts as a lateral trace-mean filter. It strives to make traces laterally more similar suppressing traces with a high mean value or amplifying those with a low mean value by multiplication with a constant factor.

3.1.4.7 NMO-correction

The two-way-travel time (TWT time) is the time the signal needs from the transmitter down to the reflecting horizon and up again to the receiver. The TWT time measured with the common-offset method is slightly longer than the one used in processing because of the distance between

transmitting and receiving antenna. This has to be corrected for by using the antenna distance and an assumed average subsurface velocity, in this case 0.1m/ns.

3.1.4.8   Phase-shift migration

For the sake of simplicity it usually is assumed that a reflection is coming from directly below the GPR device. But this is of course only the case if the reflector is horizontal. In the case of a point source or a dipping reflector this assumption leads to diffraction hyperbolas or lines which are dipping too steep. Migration is one of the most powerful processing tools. It will collapse diffraction hyperbolas back into one point and correct for the false dip of lines.

Phase-shift migration in particular is a frequency-wavenumber method and assumes constant subsurface velocity. The real subsurface velocity is generally about 15% higher than the average subsurface velocity gathered from migration. This fits quite well with the obtained migration velocity of 0.08m/ns which lies in a 15% range of the assumed real subsurface velocity of 0.1m/ns.

3.1.4.9   F-k filter

For this filtering technique the data is transformed from the t-x domain (time-distance) to the F-k domain (frequency-wavenumber). There, similar to the band-pass filter but in 2D, parts of the F-k plane are muted leaving only a narrow fan. The F-k filter was only used to remove steeply dipping migration artefacts.

3.1.4.10   F-x deconvolution

This filter makes use of the fact that noise contrary to the desired signal is usually totally random. Therefore one trace can be predicted by comparing it to previous traces in the F-x domain. The part of the prediction which holds true is assumed to be the desired signal and will be attenuated. The other part is assumed to be noise and will be suppressed.

3.1.4.11   Topographic correction

Up until now all traces would start at the same time-zero position, which would distort features in the subsurface. To adjust for this, each trace will be pulled up to its correct position appointed by DGPS measurement using the above gained velocity information (0.1m/ns).

3.1.4.12 Time-to-depth conversion

Finally, for an improved understanding of the actual depth of horizons, the timescale will be converted to depth by means of the average subsurface velocity (0.1m/ns).

3.2 Differential Global Positioning System (DGPS)

3.2.1 Basic principle and acquisition setup

GPS allows one to calculate a three-dimensional position by contacting a minimum of four satellites and measuring the travel time of its signal to each one of them [*King et al.*, 1996]. The received signal though suffers from at least two types of errors: a clock error if either the travel time is incorrect or an orbit and atmospheric error if the satellite position is incorrect [*King et al.*, 1996]. Until May 2000 there was also a third type of error called Selective Availability (SA): The random downgrading of GPS signal by the United States Department of Defence [*Adrados et al.*, 2002].
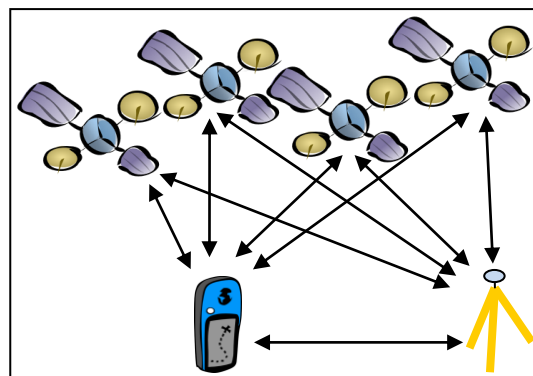
Figure 3.5: Schematic DGPS measurement situation with measuring device, base station and four satellites.

By introducing a second GPS antenna, called base station, which suffers from the same orbit and atmospheric errors as the measuring antenna, this errors can be minimised and thus the accuracy optimised [*Adrados et al.*, 2002].

3.2.2 Data acquisition

During GPR data gathering the GPR sledge was equipped with a GPS antenna. For the 100MHz GPR dataset the corresponding GPS data was acquired with the NovaTel DGPS system. For the 250MHz GPR dataset the Leica DGPS system was used.

Between the two GPS datasets there could be observed a shift in all three coordinates. A probable reason is the use of two different DGPS measuring systems.

The GPS data was used (1) during processing of the GPR data and (2) for a 3D topography model of the study area. The topography model was made with Matlab by interpolating between the measured lines given in the CH1903 (Swiss) coordinate grid (see figure 1.1).

3.3 Soil profiles

On June 10th 2010, 6 soil profiles, H1-H6 in figure 1.1, were dug up in the study area at strategically important points to gain some more information and certainty about different horizons and their depth. For detailed information see table 8.2.

Figure 3.6: Three soil profiles were dug up at each side of the past landslide. In the landslide mass was found schist and mica.

4   Results

4.1   DGPS topography
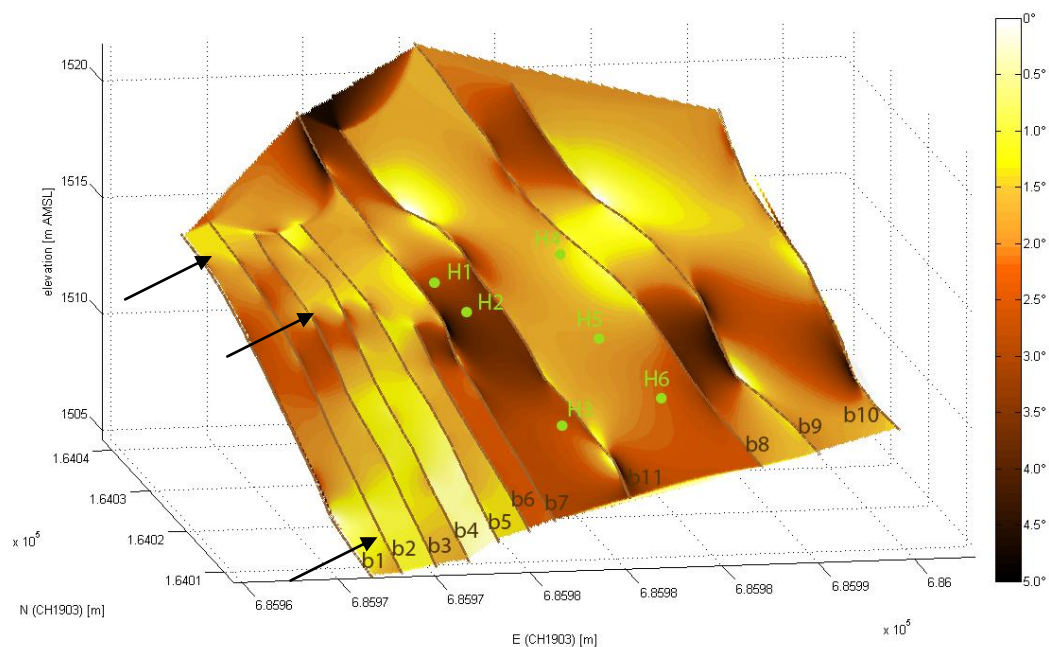
Figure 4.1: Topography map of the upper part of the study area with colour indicating slope. Black arrows mark the location bumps.

The strongly disrupted surface of the past landslide (between soil profiles H1-H6 in figure 3.3) is of no interest for topography analysis. The part right of the landslide does not seem to have too strongly changing topography. Still the upper part is somewhat flatter, showing in yellowish colours in figure 4.1, which could be the continuance of the ridge which is followed by line a4.

Looking at the left side of the landslide the change in topography is rather surprising. The general trend of the slope stays the same but now many more ridges on a smaller scale can be observed (marked by black arrows). The whole slope seems to gently undulate which can be seen in figure 4.1 from the alternately yellow and red patches.
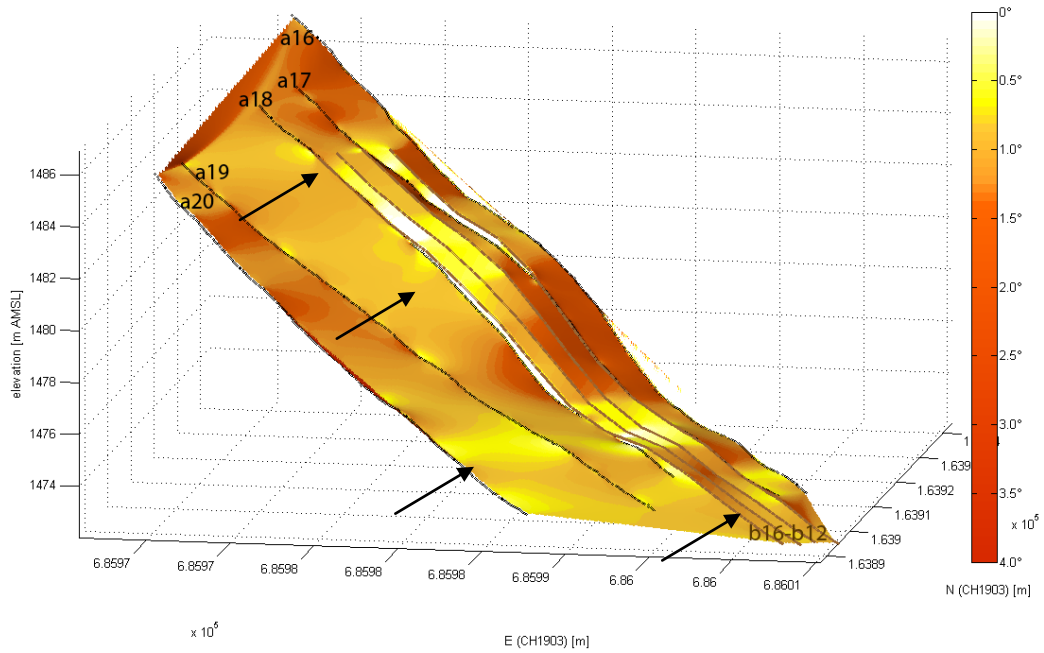
Figure 4.2: Topography map of the lower part of the study area with colour indicating slope. Black arrows mark the location of bumps.

This lower part shown in figure 4.2 is shallower all in all but seems to have a similar noticeable topography as mentioned above. Small ridges or waves can be observed (marked by black arrows).

4.2 GPR profiles

Figure 4.3: Picture of the upper part of the study area, taken on the 28th of July 2009.

As mentioned above the investigation area can be roughly split up into an upper steep part U1-U3 and a lower flatter part L (see figure 3.3). This picture (figure 4.3), taken on the 28th of July 2009, gives a good overview over the whole situation of the upper part. In the middle, labelled U2, the past landslide from spring 2008 can be easily recognised by the missing patches of grass. In part U3 the sward is also broken up, this looks like an older landslide. The area U1 is assumed to be actively creeping as cracks were observed in the soil.

It can be seen in profile a3 (figure 4.4) that the penetration depth of the 100MHz GPR increases significantly from around 5m in the steeper part to over 10m in the less steep part. Interestingly this deepening trend of the penetration depth cannot only be seen toward the flatter part but also in the cross line profile a4 (figure 4.5) where the penetration depth varies between 5m and 10m.
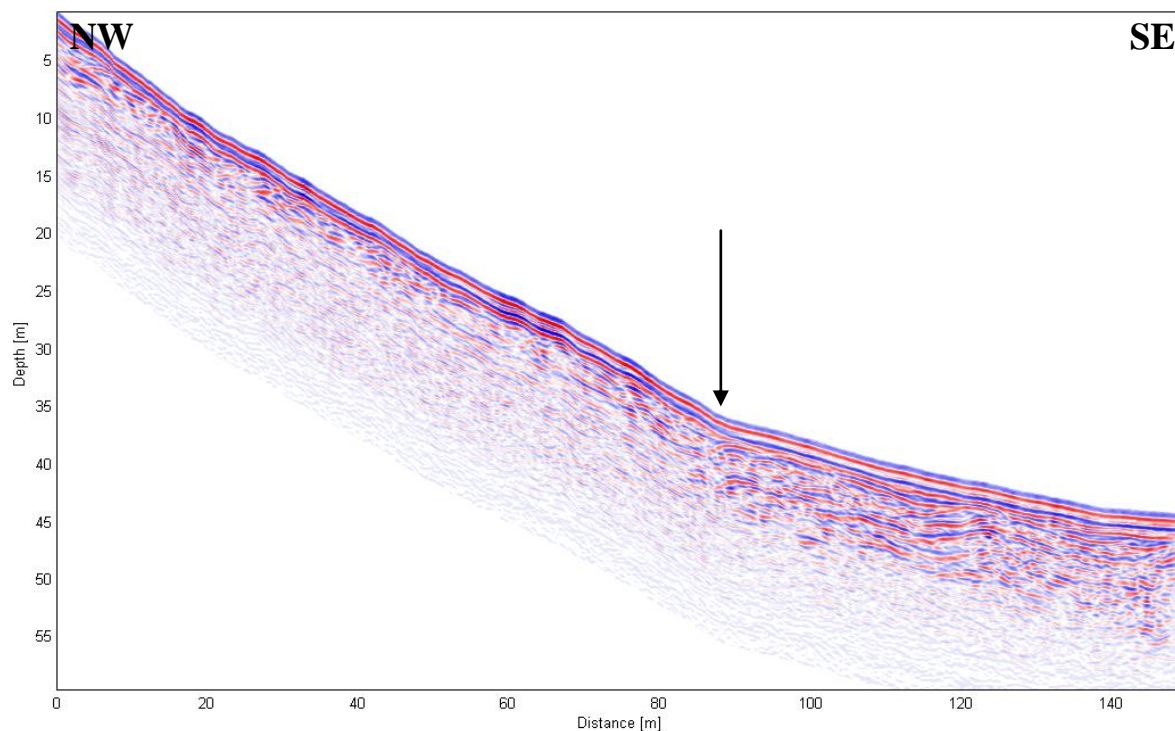
Figure 4.4: 100MHz GPR profile of line a3 with scale 1.5:1. The black arrow marks the change in georadar facies.

Also visible in figure 4.4 is the transition in the georadar facies (marked with a black arrow) between the steeper and the flatter part. The flatter part is characterised by large sigmoidal structures. The upper part seems to be more linear or shows sigmoidal structures on a smaller scale. Both facies will be discussed in detail further below.
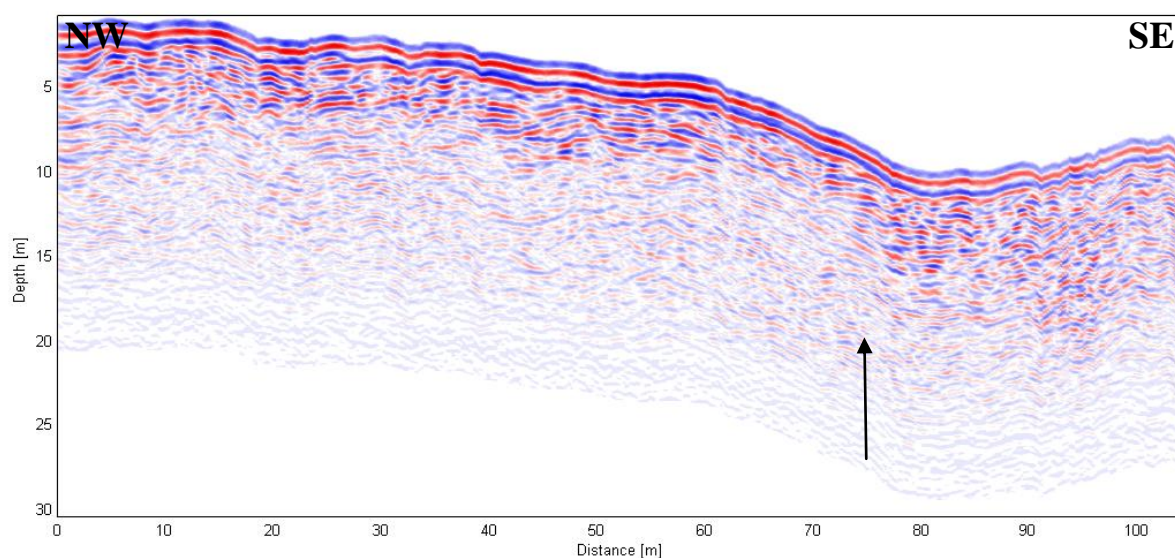
Figure 4.5: 100MHz GPR profile of line a4 with scale 1.5:1. The sudden increase in depth penetration is marked with a black arrow.

4.2.1 Area U1: upper steep part left of the past landslide
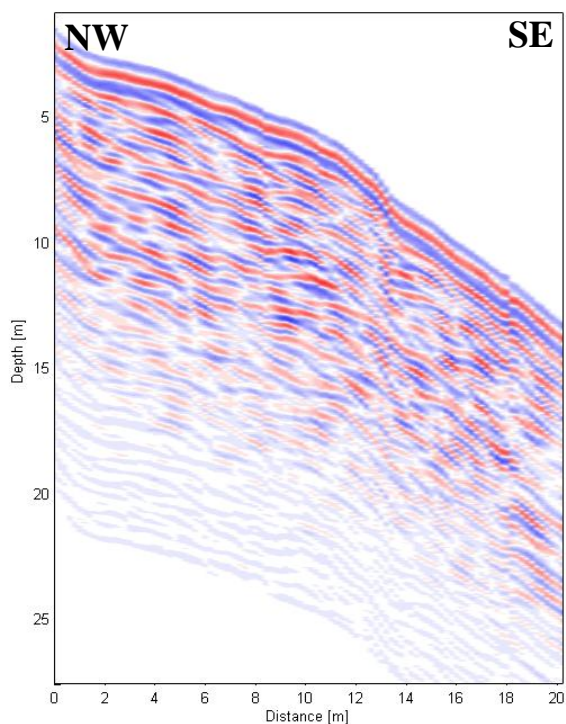
Figure 4.6: 100MHz GPR profile of line a9 with scale 1:1.

First thing to notice is that depth penetration in this area U1 seems to be quite constant without any sudden drops. This is to say for the 100MHz profile of line a9 (figure 4.6) it reaches around 12m and for the 250MHz line b7 (figure 4.7) it is about 5m. Note that this is at least twice the depth of what would be expected from the 100MHz line in figure 4.4. This could either be a processing effect or depth penetration increases not only from top to bottom as mentioned above but also from east to west which is supported as well by figure 4.5. In the 250MHz profiles b1-b7 though there can be seen temporary decreases in depth penetration like wholes or domes (see figure 5.4).

As briefly mentioned above this upper part U1 also has its own georadar facies. In figure 4.6, the 100MHz profile of line a9, some nearly linear parts seem to alternate with cross-beded sequences.

In profile b7 (figure 4.7) breaks and disruptions of the ground-wave can be noticed in several places at the surface.

Finally a more or less continuous first strong reflection can be observed. Below this first strong reflection several bright spots can be noticed.
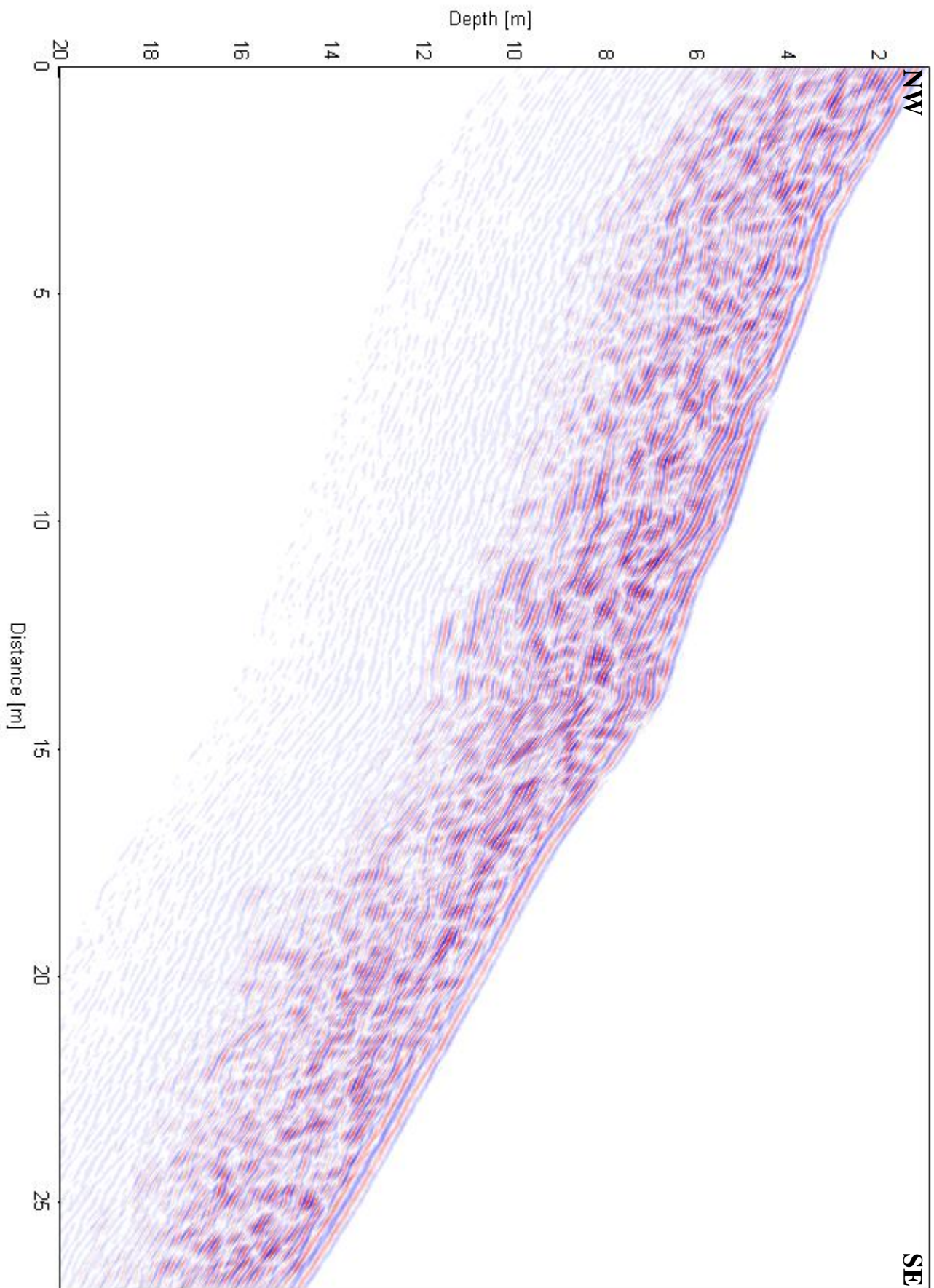
Figure 4.7: 250MHz GPR profile of line b7 with scale 1.5:1.

4.2.2 Areas U2 and U3: upper steep part, past landslide areas
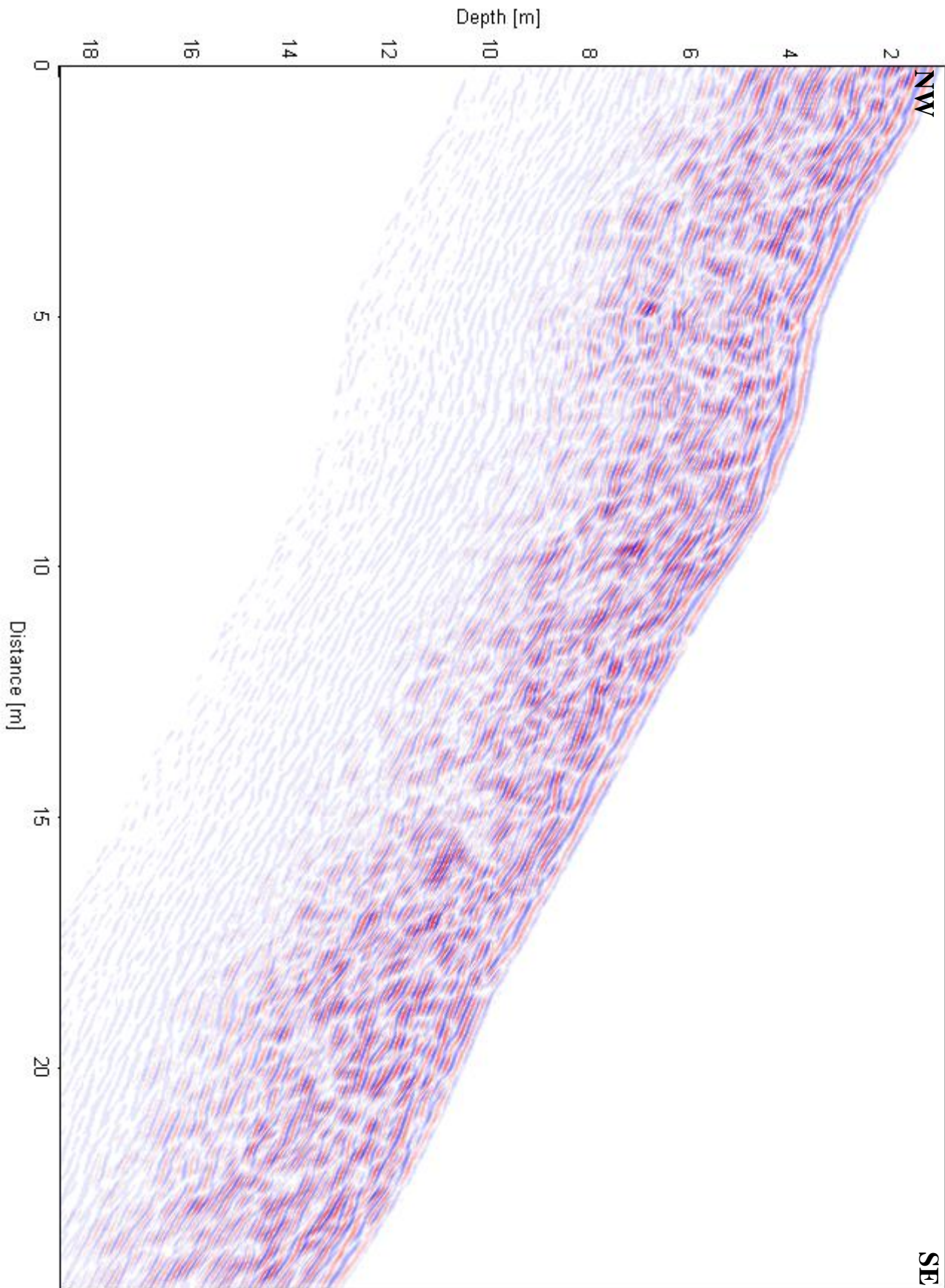
Figure 4.8: 250MHz GPR profile of line b11 with scale 1:1.

Areas U2 and U3, the part with the past landslide and the part directly right of it, seem to have a very similar georadar facies compared to area U1. Although less linear sequences can be found in profile b11 (figure 4.8) and the ground-wave is disturbed in even more places. A few bright spots can be seen but no continuous strong reflection.

Profile b10 (figure 4.9) is more linear than profile b11. In this profile as well the ground-wave is disturbed but only in some distinct places. Still the observed bright spots cannot be connected to a continuous strong reflection.
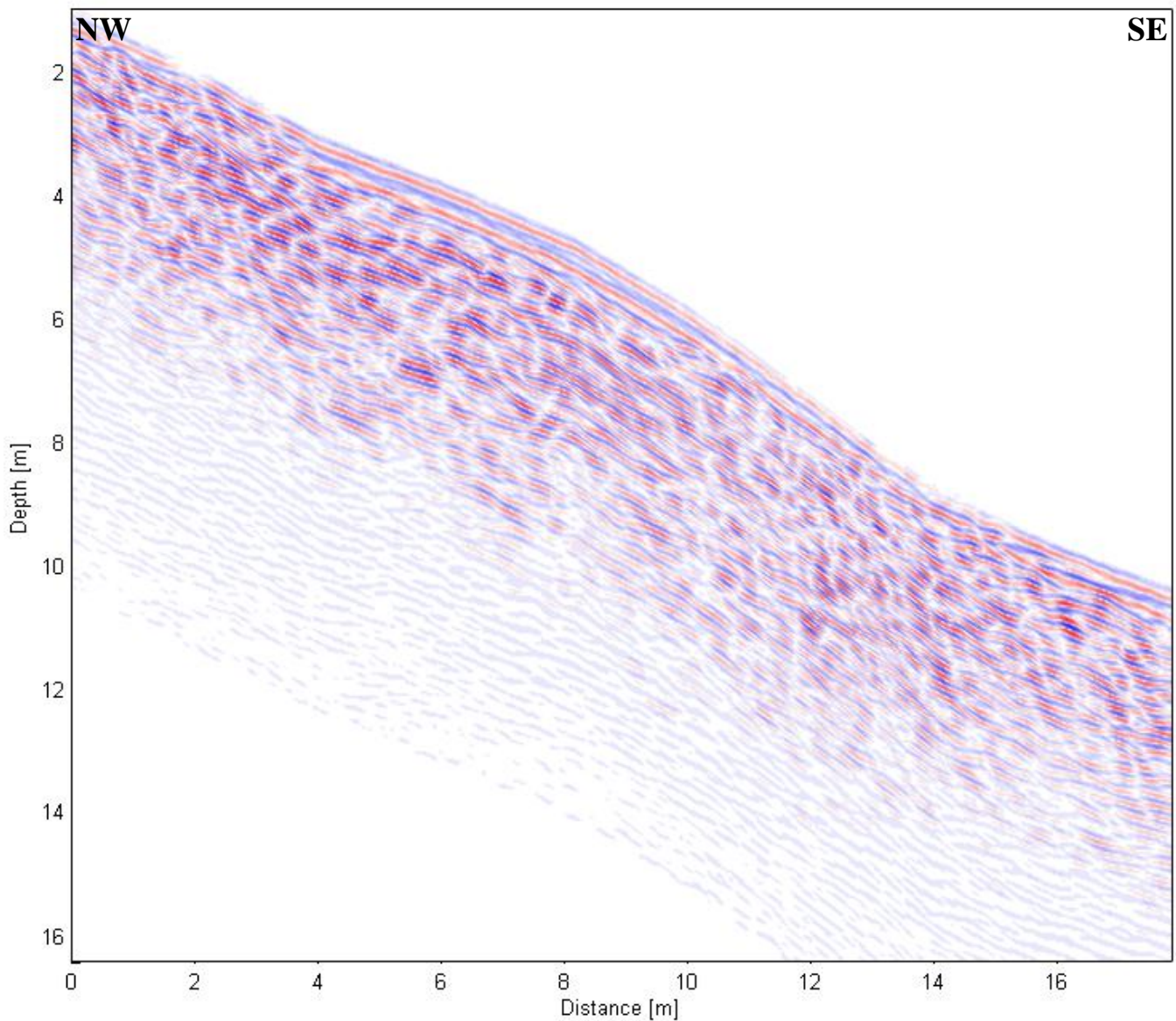
Figure 4.9: 250MHz GPR profile of line b10 with scale 1:1.

4.2.3 Area L: flat part
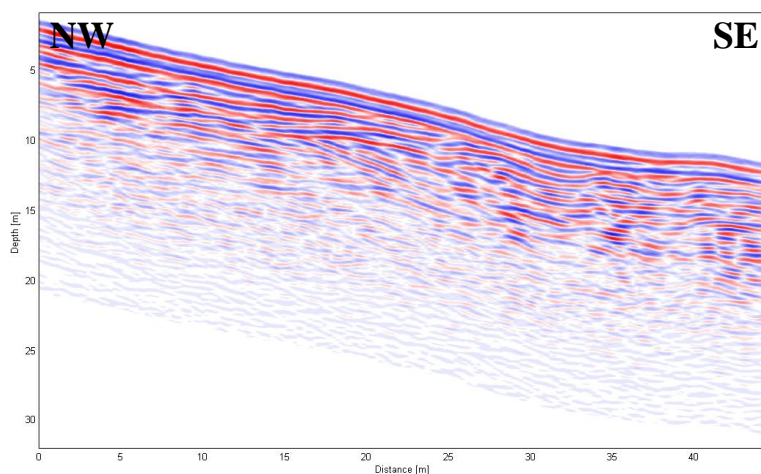
Figure 4.10: 100MHz GPR profile of line a18 with scale 1:1.

As mentioned above the depth penetration in this area is rather deep compared to the steeper part. The last strong reflections lay in around 10m depth with a 100MHz frequency and around 6m depth with a 250MHz frequency.

Area L can be described by more or less all the same georadar facies. Already from the less well resolved 100MHz profile (see figure 4.10) large sigmoidal structures can be observed. Reflections tend to appear out of the subsurface and at some point disappear into the ground wave. There can also be observed a certain trend to build packages or bundles of sigmoidal reflections which are then in a flat angle cut off by new bundles of reflections. The topography although gently undulating as well seems not to follow the structures in the subsurface or at least not strictly. Finally there can be identified around four nearly equally very strong reflections in of profile b16 which are extremely well defined and can be followed over the whole profile.
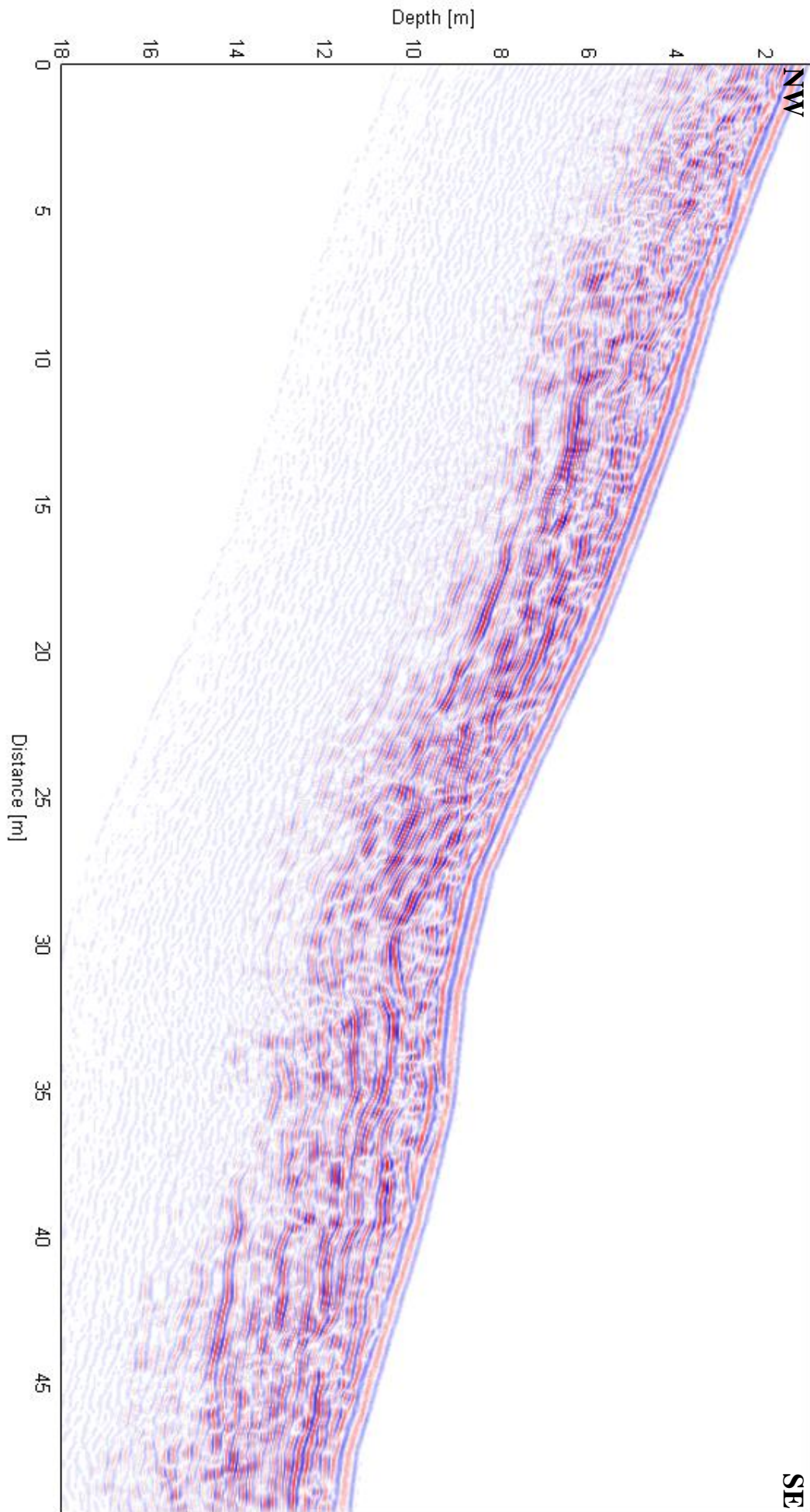
Figure 4.11: 250MHz GPR profile of line b16 with scale 1.5:1.

4.3 Soil profiles
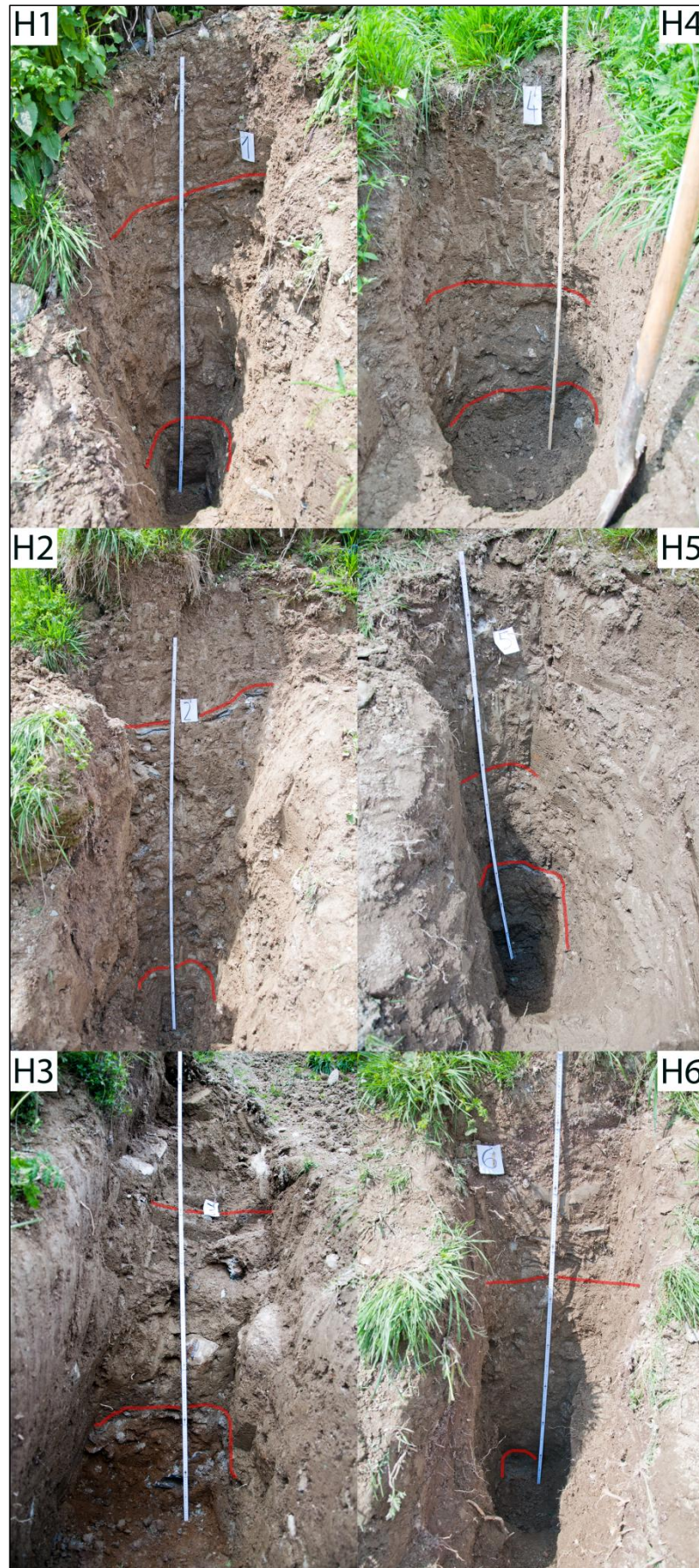
Figure 4.12: Soil profiles H1-H6 with clay layer (lower red line) and schist layer (upper red line) marked (see table 8.2 for more information)

The top soil layer has a small stone content (<10%) and consists of loamy sand (Sl). In about half a meter depth a rather abrupt increase in stone content to sometimes over 50% can be observed. The stones found in this 'schist layer' are all sericite or chlorite mica schist. They are strongly weathered and 'imbricated', meaning all of the stones follow a
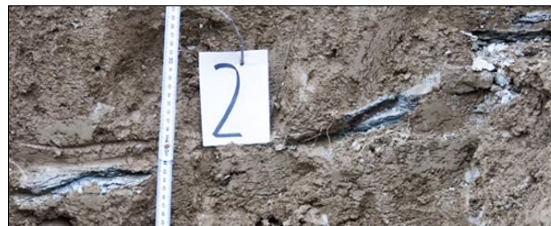
Figure 4.13: Detail from soil profile H2. Schist layer with imbricated mica.

certain dip, in this case more or less the surface. This is interesting because the layering of the bedrock is nearly perpendicular to the surface. So there seems to be some other process at work here. Below the schist layer the stone content decreases again to less than 10%.

Figure 4.14: Clay clump from one of the soil profiles. Mark the orange and grey stripes.

With increasing depth the soil gets more and more clayey (Ts). Orange and grey coloured spots and stripes can be observed (see figure 4.14). At about 1.50m a grey, only a few centimetres thin band stands out quite clearly, consisting of nearly only pure clay (T) with some sand. The clay layer as well follows the surface with its inclination which can be nicely seen in figure 4.15. Below the clay layer the clay content decreases somewhat but still stays high (Ts).

Of further interest is also the varying depth in the different soil profiles. Comparing profiles H1, H2 and H3, which were dug up just below each other, one can see that the clay layer comes up in profile H3 but the schist layer has a downward trend from top to bottom. In profiles H4, H5 and H6 laying on the other side of the landslide the clay layer has a downward trend but starting from a higher level than in profiles H1-H3. The schist layer stays more or less at the same depth. It is also noticeable that the schist layer is much less well defined in profiles H4-H6.

Figure 4.15: Detail from H5. The clay layer is well visible as a fine grey and inclined band.

5 Discussion

5.1 Creeping behaviour
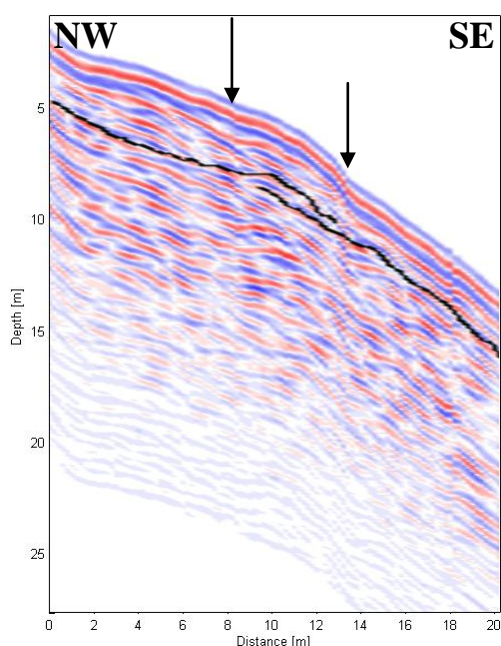
Figure 5.1: 100MHz GPR profile of line a9 with interpretation in black and scale 1:1.

The above observed cross-beded facies in the centre of profile a9 between the two more linear sequences (between the two black arrows in figure 5.1) can be interpreted as layers which are overthrusted in this part because of some stress from above. The small bump in topography supports this as well.

In profile b7 which has been taken with the 250MHz GPR device at nearly the same place as a9 some similar features can be observed. The lowest identifiable and less strong horizon is probably the beginning of the bedrock as it was observed in the soil profile H1-H3 (see figure 4.12 and table 8.2). The next higher horizon and the in chapter 4.2.1 mentioned strong reflection is assumed to be the clay layer as clay would give the desired strong reflection and the clay layer seems to be a although thin but continuous layer. The uppermost horizon could be the schist layer detected in the soil profiles.

Even though a clay layer was found in both the GPR and the soil profile it seems that in this particular location of area U1 the clay layer is maybe too deep to act as a gliding plane. But on the other hand the schist seems to have acted as a gliding plane for the past landslide already because the new elevation of the past landslide area is at about the depth of the schist layer in the soil profiles and schist and mica can be found all over the past landslide mass. This opens an interesting new perspective as now both clay and schist come into consideration for an active gliding plane.

As can be seen in figure 5.2 both possible gliding planes have a rather rough topography. Also the surface topography is quite bumpy and the disturbed ground-wave indicates at cracks in the ground. All these factors together seem to speak for a part by part motion where one package of soil is thrusted into the one below and thus opening a small crack above making room for the next package. Steps in the gliding plane topography keep packages locked for some time and prevent the soil from rushing down. This enables the whole slope to slowly creep downwards. The steps in the gliding plane might have been built by the push and pull of landslides moving over it.
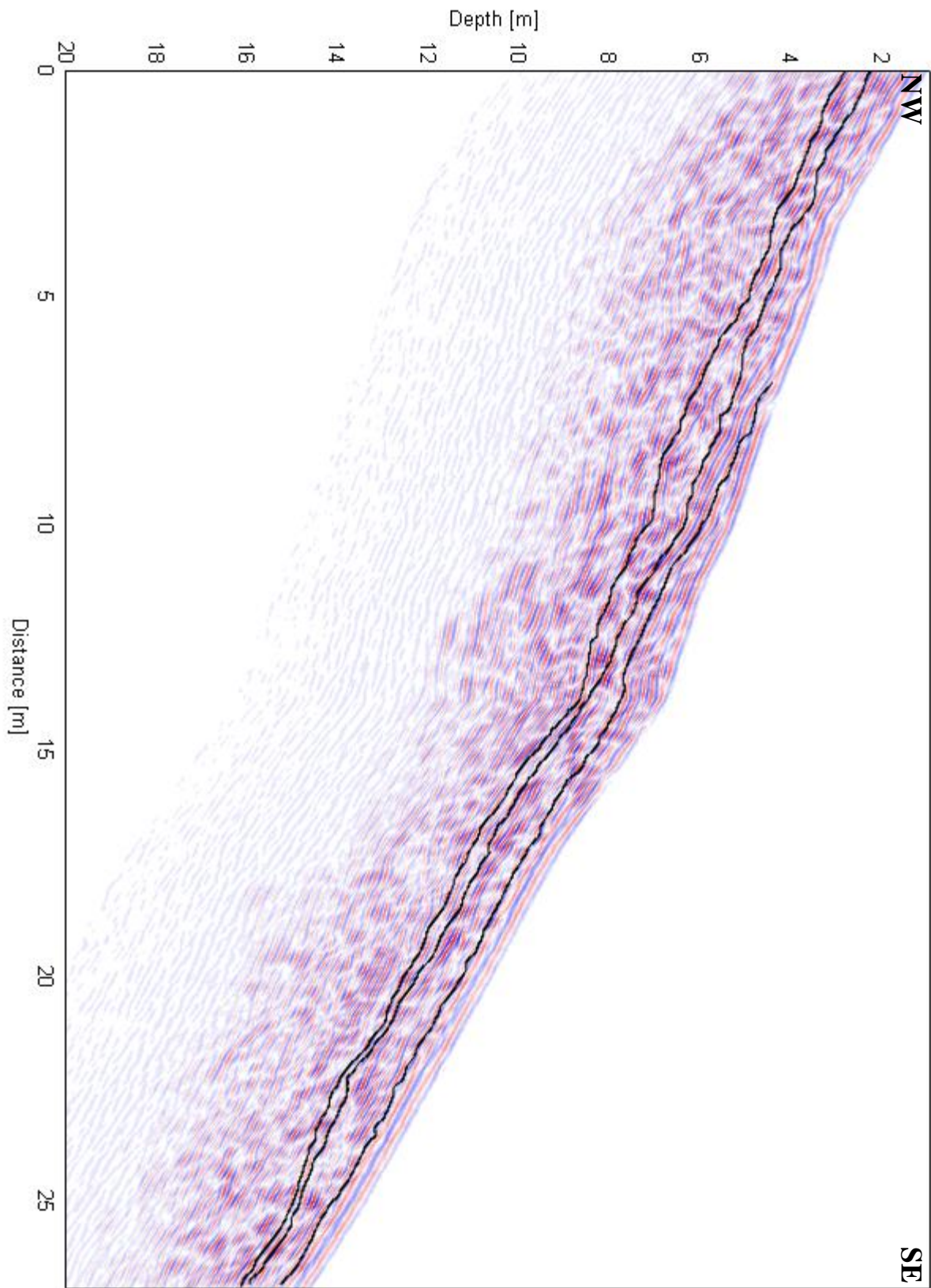
Figure 5.2: 250MHz GPR profile of line b7 with interpretation in black and scale 1:1.

5.2 Remnants of the Axen fault?
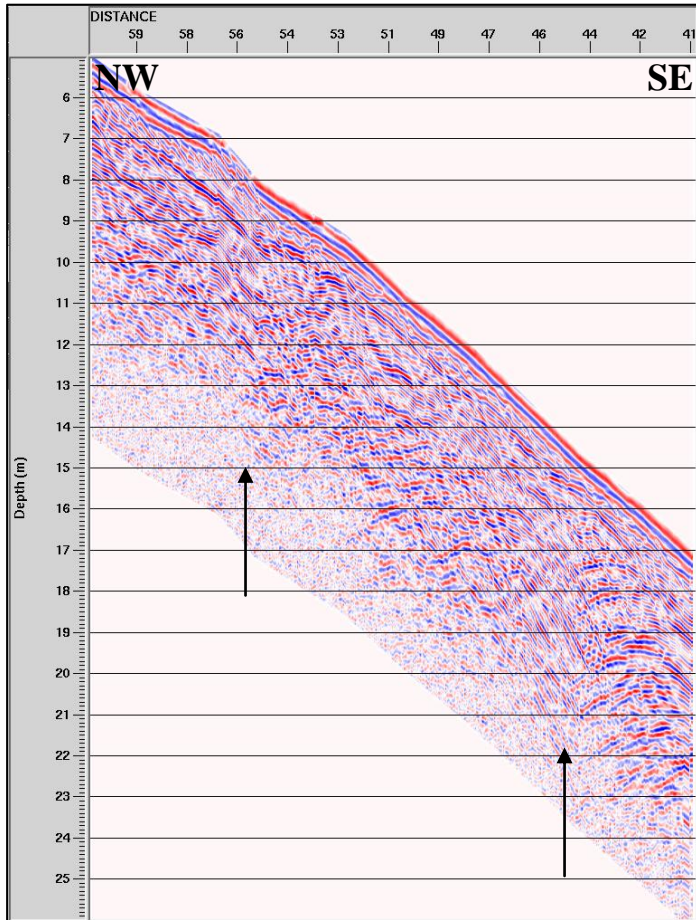
Figure 5.3: 250MHz GPR profile of line b3, unmigrated, with scale 1.5:1. The black arrows mark the position of crossed reflections.

In some profiles (figure 5.4) a sudden short decrease in depth penetration can be observed. In the unmigrated section the same part is represented by crossed lines (see figure 5.3 the black arrows), which is usually a sign for a fault. These supposed faults though seem to penetrate deep into the bedrock. Therefore much more force is needed than a landslide.

A possible source could be the near major fault zone: the Axen fault. It separates the Urseren Zone from the Aare massif and lies only a few hundred meters upslope. As the Axen fault is not active any more, subfaults would only show up in the bedrock.
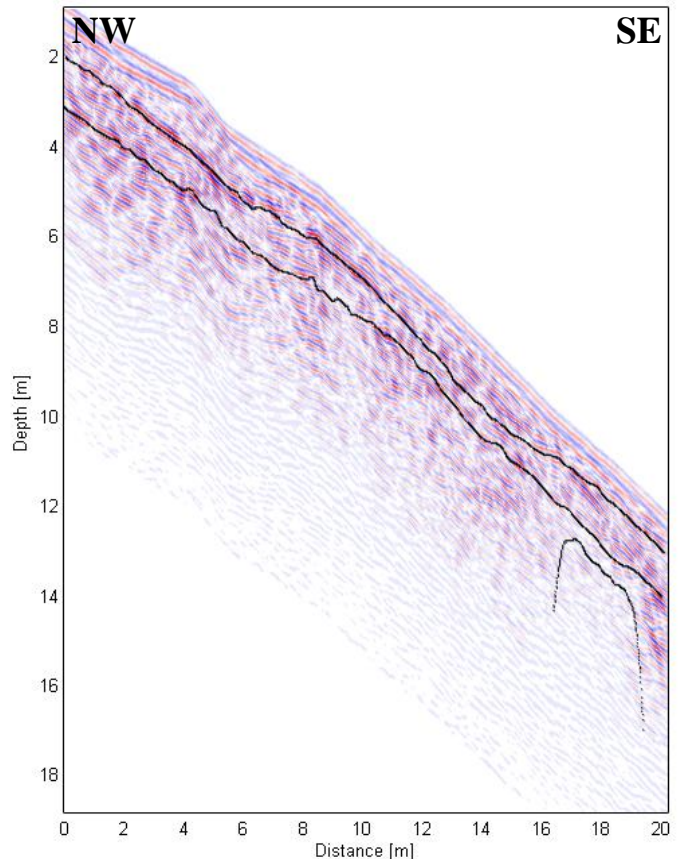
Figure 5.4: 250MHz GPR profile of line b3 with scale 1.5:1. A sudden decrease in penetration depth can be observed.

31

5.3   Westward migrating creeping regime

From the picture in figure 4.3 it seems that the easternmost area U3 is built up from a landslide past a few years ago. In the area U2 in the middle on the other hand can be observed a two year old landslide deposit and the area U1 to the west is still actively creeping and expected to rush down some time in the near future. All in all there seems to be a westward migration of the creeping regime.

This is also supported by the georadar profiles of this area. Profile b11 (figure 4.8) taken in area U2 shows nearly no strong reflecting horizons which speaks for a strongly disrupted subsurface. Also the many breaks of the ground-wave show the perturbed surface. In comparison profile b10 (figure 4.9) with its more linear but still weak reflection and less disrupted ground-wave might well show an older landslide where the soil building processes are already further progressed.

It was also observed that the schist layer in soil profiles H4-H6 is less well developed and imbricated than in profiles H1-H3. This could be the case because this schist layer was already used as a gliding plane for the old landslide in area U3 and thereby was disrupted. Also it seems that the past landslide in area U2 used the same schist layer as a gliding plane as the landslide mass was covered in schist and mica (see figure 3.6).

5.4 Landslide cemetery model
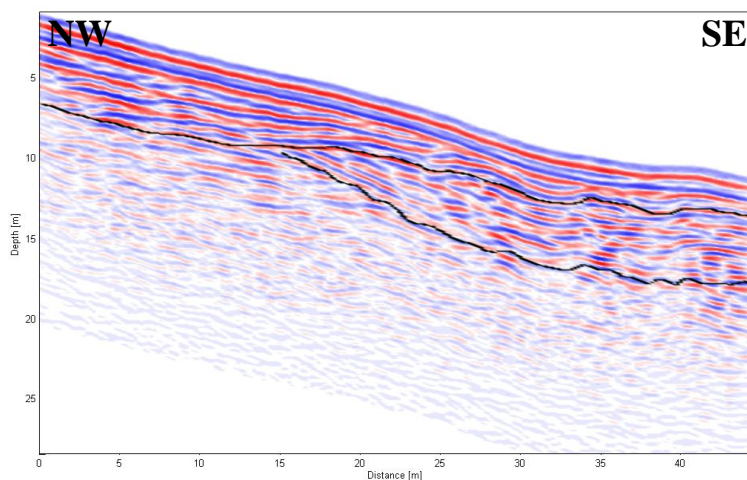
Figure 5.5: 100MHz GPR profile of line a18 with interpretation in black and scale 1:1.

Gathered from the soil profile there should be only three strong reflections: bedrock, clay layer and maybe the schist layer. One explanation why there can be seen more than three stronger reflections in figure 5.6 is that the clay layer or schist layer appears more than once in the profile. This condition could be accomplished by multiple landslides being deposited at the same place over a long time: The landslide cemetery.

The sudden decrease in slope causes the landslide to stop at the same place. With enough time new soil is rebuilt by alluvial acquisition and soil building processes. At the landslide deposition site soil is built as well and with it a new clay layer. After enough time a new landslide will rush down at exactly the same location burying the old landslide deposits together with its clay layer. This will lead to multiple clay layers and massively increased depth to bedrock at the landslide deposition site which shows itself in an increased penetration depth.

A landslide which is creeping slowly or rushing down momentarily will create a push on the stack of old landslide from the hillside. This could if the push is strong enough even lead to folding up of either the whole stack or separate layers. The multiple clay layers could in this case act as fault planes.
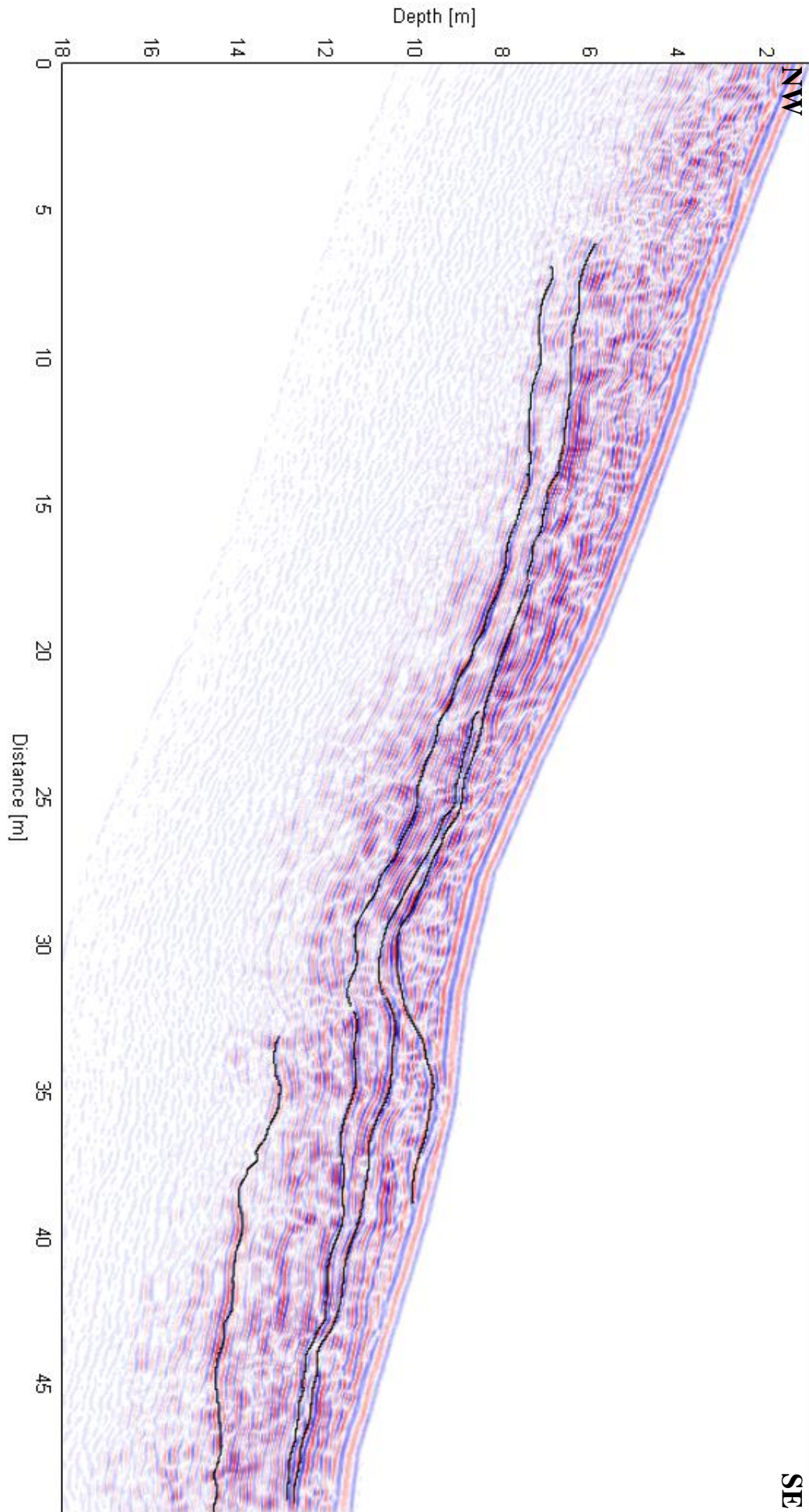
Figure 5.6: 250MHz GPR profile of line b16 with interpretation in black and scale 1.5:1.
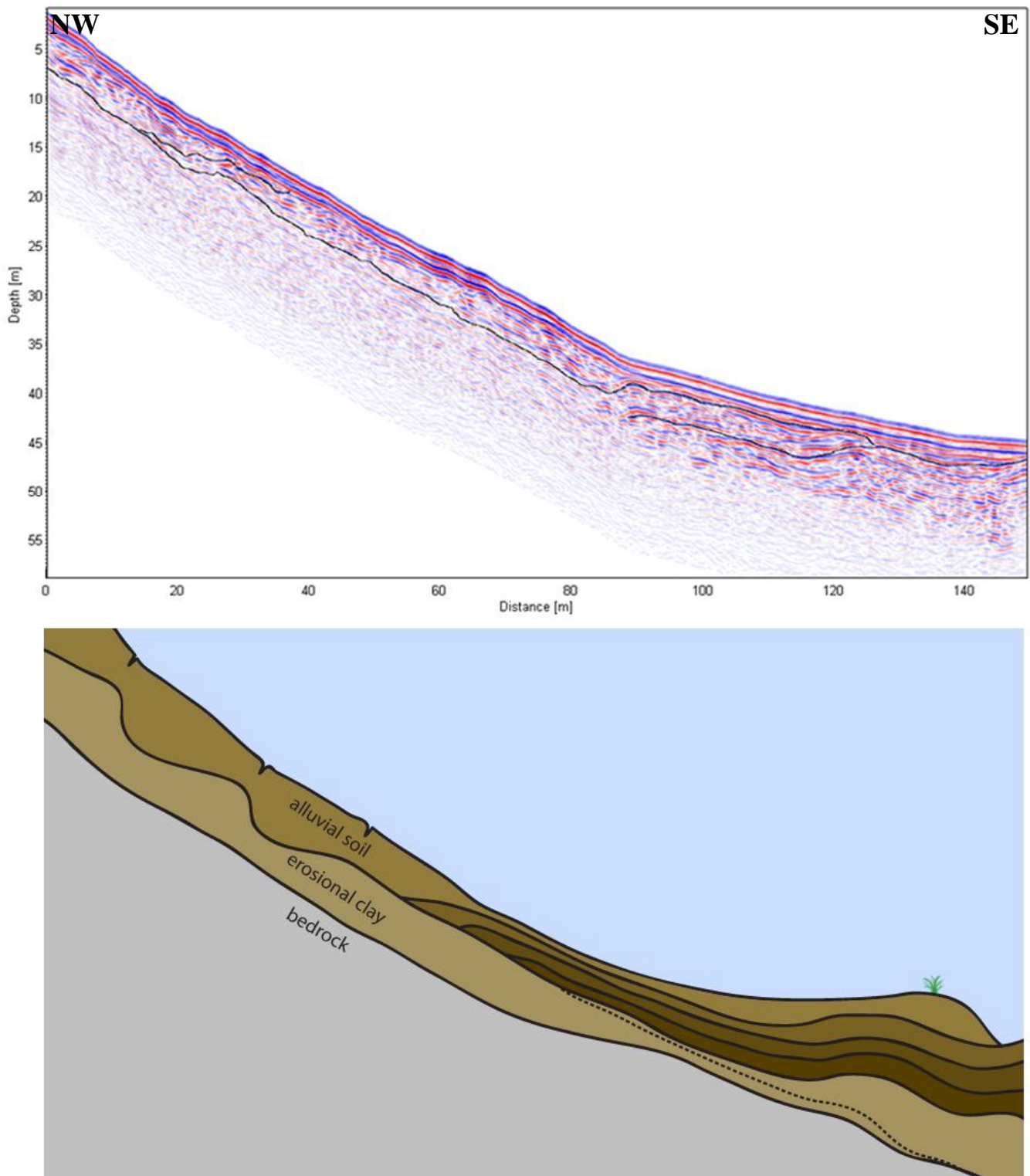
Figure 5.7: a) 100MHz GPR profile of line a3 with interpretation in black and scale 1.5:1.
b) Final model for whole study area with upper part as landslide source area where soil is gathered by soil building and alluvial processes and the lower part as 'landslide cemetery' where multiple landslides are deposited and build a thick layer with multiple clay layers. The dashed line marks the original clay layer.

6   Conclusions and outlook

As expected from the cracks visible at the surface, the landslides in the investigation area seem to follow a part by part movement thus slowly creeping downwards. But the additional data gathered like the soil profiles, GPS topography information and GPR profiles of the flatter part show a glimpse of a much more complicated story.

Is there really a westward migration of the creeping regime and what exactly is the role of the Axen fault? This questions can probably only be solved by a full 3D survey.

Another interesting question which was left open is the time and mechanism of failure. This question can be approached by a water flow model where the water flow between the surface and the assumed gliding plane is modelled. This method is bound to deliver some interesting results as the gliding plane topography (see figure 5.2) is folded into steps and pools.

7   References

Adrados, C., I. Girard, J.-P. Gendner, and G. Janeau (2002), Global Positioning System (GPS) location accuracy improvement due to Selective Availability removal, *Comptes Rendus Biologies*, *325*(2), 165-170.

Annan, A. P. (2009), Electromagnetic Principles of Ground Penetrating Radar, in *Ground Penetrating Radar Theory and Applications*, edited by M. J. Harry, pp. 1-40, Elsevier, Amsterdam.

Blume, H.-P., et al. (Eds.) (2002), *Lehrbuch der Bodenkunde*, 15th ed., 593 pp., Spektrum Akademischer Verlag GmbH, Heidelberg.

Cadisch, J., P. Niggli, R. Rutsch, H. Gunzler-Seiffert, H. Huttenlocher, C. Burri, E. Wenk, and M. K. Wells (1948), An account of the long field meeting held in Switzerland: 6th-21st September, 1947, *Proceedings of the Geologists' Association*, *59*(4), 181-228, IN181-IN187.

Cassidy, N. J. (2009), Ground Penetrating Radar Data Processing, Modelling and Analysis, in *Ground Penetrating Radar Theory and Applications*, edited by M. J. Harry, pp. 141-176, Elsevier, Amsterdam.

Fehr, W. (1926), Geologische Karte der Urserenzone, Kommissionsverlag: A. Franke A.G., Bern.

Institut für Geologie der Universität Bern (2005), Geologische Karte der Schweiz, Bundesamt für Wasser und Geologie, Bern-Ittigen.

King, B. A., S. G. Alderson, and D. Cromwell (1996), Enhancement of shipboard ADCP data with DGPS position and GPS heading measurements, *Deep Sea Research Part I: Oceanographic Research Papers*, *43*(6), 937-947.

Lacasse, S., and F. Nadim (2009), Landslide Risk Assessment and Mitigation Strategy, in *Landslides; Disaster Risk Reduction*, edited, pp. 31-62, Springer Verlag, Heidelberg.

Meusburger, K. (2009), Soil erosion in the Alps - Causes and Risk assessment, Inauguraldissertation thesis, 139 pp, Basel, Basel.

Meusburger, K., and C. Alewell (2008), Impacts of anthropogenic and environmental factors on the occurrence of shallow landslides in an alpine catchment (Urseren Valley, Switzerland), *Nat. Hazards Earth Syst. Sci.*, *8*(3), 509-520.

Pfiffner, A. O. (2009), *Geologie der Alpen*, 1st ed., 357 pp., Haupt Verlag, Bern.

8 Appendix

lines:	description:	traces:	length [m]
a1	long line, overview	397	79.4
a2	"	793	158.6
a3	"	749	149.8
a4	long line, across	523	104.6
a5	short line, unused	40	8
a6	"	70	14
a7	"	43	8.6
a8	short line, top, steep part, right, U3	105	21
a9	short line, top, steep part, unstable area U1	102	20.4
a10	short l., top, steep part, past landslide area U2	249	49.8
a11	short line, top, steep part, unstable area U1	52	10.4
a12	"	159	31.8
a13	"	76	15.2
a14	"	76	15.2
a15	"	424	84.8
a16	short line, bottom, flat part L	276	55.2
a17	"	244	48.8
a18	"	223	44.6
a19	"	221	44.2
a20	"	212	42.4
b1	short line, top, steep part, unstable area U1	398	19.9
b2	"	413	20.65
b3	"	405	20.25
b4	"	381	19.05
b5	"	385	19.25
b6	"	238	11.9
b7	"	538	26.9
b8	short line, top, steep part, right, U3	571	28.55
b9	"	506	25.3
b10	"	378	18.9
b11	short l., top, steep part, past landslide area U2	509	25.45
b12	short line, bottom, flat part L	985	49.25
b13	"	992	49.6
b14	"	992	49.6
b15	"	994	49.7
b16	"	988	49.4

Table 8.1: Details and short description of the acquired GPR data lines.

profile	H1	H2	H3	H4	H5	H6
depth h1 (cm)	0-20	0-60	0-80	0-15	0-25	0-25
soil type h1	SI	SI	SI	Ts	SI	SI
pH h1	<5	<5	<5	<5	<5	<5
stone content h1 (%)	<10	<10	<10	<10	<10	<10
LD h1	1	1	1	1	1	1
notice	NA	NA	NA	old slide horizon	NA	NA
depth h2 (cm)	20-50	60-75	80-145	15-70	25-85	25-75
soil type h2	Ts	Ts	Ts	Ls	Ts	Ts
pH h2	<5	<5	<5	<5	<5	<5
stone content h2 (%)	<10	<10	<10	<10	<10	<10
LD h2	1	1	1	1	2	2
notice	A and B horizon not distinguishable	A and B horizon not distinguishable	Schist layer starts at 80cm, A and B horizon not distinguishable	NA	NA	A and B horizon not distinguishable
depth h3 (cm)	50-115	75-190	145-185	70-120	85-160	70-150
soil type h3	Ts	Ts	Ts	Ts	Ts	Ts
pH h3	<5	<5	<5	<5	<5	<5
stone content h3 (%)	~50	<40	>50	<30	<30	>50
LD h3	2	2	3	2	2	2
notice	Schist layer at 50cm	Schist layer starts at 75cm, oxidative and reductive processes	clay layer, oxidative and reductive processes	metamorph stones, oxidative, reductive processes	oxidative, reductive processes	Schist layer starts at 70cm, oxidative, reductive processes
depth h4 (cm)	115-190	190-225	NA	120-170	160-200	150-165
soil type h4	Ts	Ts	NA	Ts	T	T
pH h4	<5	<5	NA	<5	<5	<5
stone content h4 (%)	<30	<5	NA	<10	<10	<10
LD h4	2	3	NA	2	3	2
notice	oxidative, reductive processes	clay layer	NA	clay layer	clay layer, oxidative, reductive processes	clay layer, oxidative, reductive processes
depth h5 (cm)	190-245	NA	NA	NA	NA	NA
soil type h5	T (clay)	NA	NA	NA	NA	NA
pH h5	<5	NA	NA	NA	NA	NA
stone content h5 (%)	<5	NA	NA	NA	NA	NA
LD h5	3	NA	NA	NA	NA	NA
notice	upslope 190cm, downslope 200cm	NA	NA	NA	NA	NA
Total depth to bedrock	245	225	185	170	200	165
depth to clay layer	190-200	190	145	120	160	150
depth to schist	50	75	80	70	85	70

Table 8.2: Pedological details for soil profiles.
(courtesy of K. Meusburger)